NeuroImage 270 (2023) 119997

Contents lists available at ScienceDirect

NeuroImage

journal homepage: www.elsevier.com/locate/neuroimage

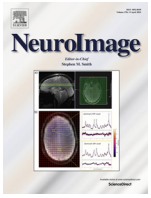

Information transmission velocity-based dynamic hierarchical brain networks

Lin Jiang[a,b,#], Fali Li[a,b,#], Zhaojin Chen[a,b], Bin Zhu[a,b], Chanlin Yi[a,b], Yuqin Li[a,b], Tao Zhang[c], Yueheng Peng[a,b], Yajing Si[d], Zehong Cao[e], Antao Chen[f], Dezhong Yao[a,b,g,h,*], Xun Chen[i,j,*], Peng Xu[a,b,*]

[a] The Clinical Hospital of Chengdu Brain Science Institute, MOE Key Lab for Neuroinformation, University of Electronic Science and Technology of China, No.2006, Xiyuan Ave, West Hi-Tech Zone, Chengdu, Sichuan 611731, China
[b] School of Life Science and Technology, Center for Information in BioMedicine, University of Electronic Science and Technology of China, Chengdu 611731, China
[c] School of science, Xihua University, Chengdu 610039, China
[d] School of Psychology, Xinxiang Medical University, Xinxiang 453003, China
[e] STEM, University of South Australia, Adelaide, SA 5000, Australia
[f] Faculty of Psychology, Southwest University, Chongqing 400715, China
[g] School of Electrical Engineering, Zhengzhou University, Zhengzhou 450001, China
[h] Research Unit of NeuroInformation, Chinese Academy of Medical Sciences, Chengdu 2019RU035, China
[i] Department of Neurosurgery, The First Affiliated Hospital of USTC, Division of Life Sciences and Medicine, University of Science and Technology of China, Hefei 230001, China
[j] Department of Electronic Engineering and Information Science, University of Science and Technology of China, Hefei 230026, China

ARTICLE INFO

Keywords:
Multimodal fusion
EEG-MRI
Information transmission velocity network
Dynamic hierarchical modulation
Performance prediction

ABSTRACT

The brain functions as an accurate circuit that regulates information to be sequentially propagated and processed in a hierarchical manner. However, it is still unknown how the brain is hierarchically organized and how information is dynamically propagated during high-level cognition. In this study, we developed a new scheme for quantifying the information transmission velocity (ITV) by combining electroencephalogram (EEG) and diffusion tensor imaging (DTI), and then mapped the cortical ITV network (ITVN) to explore the information transmission mechanism of the human brain. The application in MRI-EEG data of P300 revealed bottom-up and top-down ITVN interactions subserving P300 generation, which was comprised of four hierarchical modules. Among these four modules, information exchange between visual- and attention-activated regions occurred at a high velocity, related cognitive processes could thus be efficiently accomplished due to the heavy myelination of these regions. Moreover, inter-individual variability in P300 was probed to be attributed to the difference in information transmission efficiency of the brain, which may provide new insight into the cognitive degenerations in clinical neurodegenerative disorders, such as Alzheimer's disease, from the transmission velocity perspective. Together, these findings confirm the capacity of ITV to effectively determine the efficiency of information propagation in the brain.

1. Introduction

The human brain consists of approximately 10^{11} neurons (Shekhar et al., 2016). The information is transmitted across neurons essentially realized by the transmembrane ion flow, which generates directional currents with a finite speed and ultimately forms biological electrical activities. Generally, cognitive processes involve the activation of large neuron populations in different regions and the orderly propagation of electrophysiological signals between these regions (Panzeri et al., 2015). Whereas, clinical neurodegenerative disorders, such as Alzheimer's disease, will induce ionic imbalance, leading to dysregulated postsynaptic signal transduction and the change of neuronal information propagation (Canter et al., 2016). Therefore, the electrical potential can reflect the balanced information transmission along the axons of white matter (WM) tracts between different regions (Sousa et al., 2017). However, due to the diverse biological characteristics of WM tracts and the impaired neural circuits caused by disease, the corresponding information transmission is of

* Corresponding authors.
E-mail addresses: dyao@uestc.edu.cn (D. Yao), xunchen@ustc.edu.cn (X. Chen), xupeng@uestc.edu.cn (P. Xu).
# These authors contributed equally to this work.

https://doi.org/10.1016/j.neuroimage.2023.119997.
Received 4 November 2022; Received in revised form 9 February 2023; Accepted 27 February 2023
Available online 1 March 2023.

different efficiency across the brain areas and between healthy persons and patients, as well. Physiologically, information transmission velocity (ITV), which measures the speed of impulses traveling along the nerves, can index how fast information is transmitted between two sites. Exploring how the information propagates efficiently within the brain network has great significance, which can not only provide a new tool for understanding the underlying neural mechanism of human cognition, but also provide a new insight to probe the progressive dysfunction of neurodegenerative disorders.

Given that information is fleetly transmitted across the brain (usually in tens of milliseconds), non-invasive neuroimaging techniques such as the electroencephalogram (EEG) that can measure rapidly changing electrical activities on a millisecond scale are necessary. For example, Reed and colleagues defined the ITV of the human visual nerve pathway by dividing the maximal head length by the latency of P1 event-related potential (ERP) generated in the occipital cortex (Reed and Jensen, 1992). This ITV was further found to be correlated with individual intelligence (Reed et al., 2004). However, their study ignored the intrinsic pathway for information propagation by simply measuring the nasion-to-inion distance as the length of retino-geniculate pathway. To obtain a more precise estimation of the transmission path, Horowitz and colleagues creatively defined the mean tract length of the interhemispheric visual and tactile fibers as the path length (Horowitz et al., 2015), and the ITV was defined as the mean length of the transcallosal visual/tactile fibers divided by the difference in the latency of the N1 between contralateral and ipsilateral electrodes. Compared to early studies, Horowitz and colleagues innovatively applied diffusion tensor imaging (DTI) to estimate the propagation pathway, but the temporal factor, that is, the latency of the ERP component, was extracted from the scalp EEG. In this way, the “sending” and “receiving” sites for information propagation were positioned on the scalp and were not physiologically connected by the visual or tactile fibers, which will result in inaccurate estimation of ITV. Fortunately, EEG source reconstruction, which can project the scalp EEG signals to the source space (Bore et al., 2021; Hassan and Wendling, 2018), provides a higher temporal-spatial resolution to capture the dynamic electrical response patterns genuinely at two fiber path sites. As such, for two brain areas with direct structural fiber connectivity, the activation delay can be estimated from the source-space-projected ERP at the fiber path sites. This strategy guarantees the consistency of the spatial fiber tract determined with DTI and the temporal characteristics of information flow determined from ERP.

The human brain is an intricate network with tightly correlated structural and functional connectivity architectures (Zhang et al., 2018; Zhu et al., 2021). Most recent studies focused on the total amount of information transmission to measure the linkage strength. However, from the physiological perspective, the speed of information propagation within a network is more related to the physiological basis of neural activations. Moreover, increasing microscale evidence has demonstrated that the brain deploys populations of neurons in a temporally coordinated manner (Berkes et al., 2011; Morcos and Harvey, 2016). Namely, brain functions are often characterized by the integration of segregated large-scale subnetworks, which are facilitated by hierarchical network organizations (Demirtaş et al., 2019). However, little is known about the hierarchical network structures involved in higher-level cognitive processes. Hence, with task-activated brain regions as nodes, the construction of the cortical ITV network (ITVN) provides a golden chance for elucidating the hierarchical and dynamical functional integration in the human brain straightforwardly.

P300, a positive ERP evoked approximately 300 ms after target stimulus onset (Polich, 2007), can reflect extensive human cognition such as attention (Linden, 2005), and has been regarded as one of the biomarkers for multiple neurocognitive diseases, such as schizophrenia (Polich, 2007). As reported, balanced and efficient information transmission in the brain serves as a prerequisite of P300 and guarantees the reasonable configuration of resources (Li et al., 2020b). Consequently, P300 can be regarded as an outstanding “window” to explore the transmission mechanism of the human brain. Of note, previous studies have proven the importance of coupled bottom-up and top-down flows in regulating attention during the P300 task (Li et al., 2016), whereas their roles in hierarchically configurating related attentional resources remain unveiled. Concurrently, P300 presents a large variability across individuals (Dinstein et al., 2015; Li et al., 2020a), however, the underlying information transmission mechanism remains still unclear. Herein, by investigating the cortical ITVN, we will learn more about the inter-individual variability of P300.

Table 1
Talairach coordinates for peak voxels of activation clusters.

Anatomy	Abbreviation	Talairach Coordinates		
		x	y	z
left middle front gyrus	lMFG	−36	54	15
right middle front gyrus	rMFG	36	54	18
left inferior frontal gyrus	lIFG	−54	9	5
right inferior frontal gyrus	rIFG	50	15	4
left precentral sulcus	lPrCS	−27	−12	66
right precentral sulcus	rPrCS	42	6	45
left insula	lInsula	−41	1	0
right insula	rInsula	48	15	−5
left superior temporal gyrus	lSTG	−57	−33	22
right superior temporal gyrus	rSTG	63	−34	18
left inferior occipital gyrus	lIOG	−45	−72	−15
right inferior occipital gyrus	rIOG	39	−77	−12

Hence, in the present study, combining fiber tractography from the DTI and EEG source reconstruction, a new measure ITV was developed to determine the conduction velocity of cognitive information between two physiologically connected brain regions. After defining the regions of interest (ROIs) for the P300 task, we tracked the fiber path between each pair of ROIs, and EEG source analysis was performed to project scalp EEG into the source activities. Subsequently, the source-space-projected EEG activities at the starting and ending fiber positions were extracted to estimate the difference in P300 latency between the two fiber path ends. Based on the fiber path length and transmission interval, the corresponding ITV would be then estimated. Finally, ITVN was constructed to model the information transmission mechanism underlying the P300 response.

2. Results

2.1. Study design and overview

Before constructing the ITVN of P300, based on our previous functional MRI study (Li et al., 2020a), 12 task-activated ROIs were defined. In detail, after finishing the preprocessing of task fMRI images, generalized linear models (GLM) were applied to quantify and localize task-activated regions, and related local peaks were accordingly assessed to further extract the task-activated ROIs. Herein, according to the local peaks which showed >0 *t*-contrast in the group analysis, 12 P300-related ROIs were then defined, along with their Talairach coordinates being listed in Table 1.

Herein, we intended to combine multimodal DTI and EEG data to determine the information transmission efficiency of the human brain (Fig. 1). Specifically, based on the predefined ROIs that were spatially normalized into the standard Montreal Neurological Institute (MNI) space, we estimated the ITV between pairwise ROIs by using the DTI and EEG data to measure the fiber path length (ΔPL, Fig. 1a) and latency differences (ΔLD, Fig. 1b). As reported, a longer fiber path may correspond to a relatively higher transmission speed (Salami et al., 2003), and latency has been regarded as an electrophysiological measure of information processing speed (Kapanci et al., 2019). Namely, these two variables not only form the basis of ITV but also serve as another way to estimate transmission efficiency. Hence, besides the ITVN constructed by the ITV, for comparison, the structural network (SN) and temporal

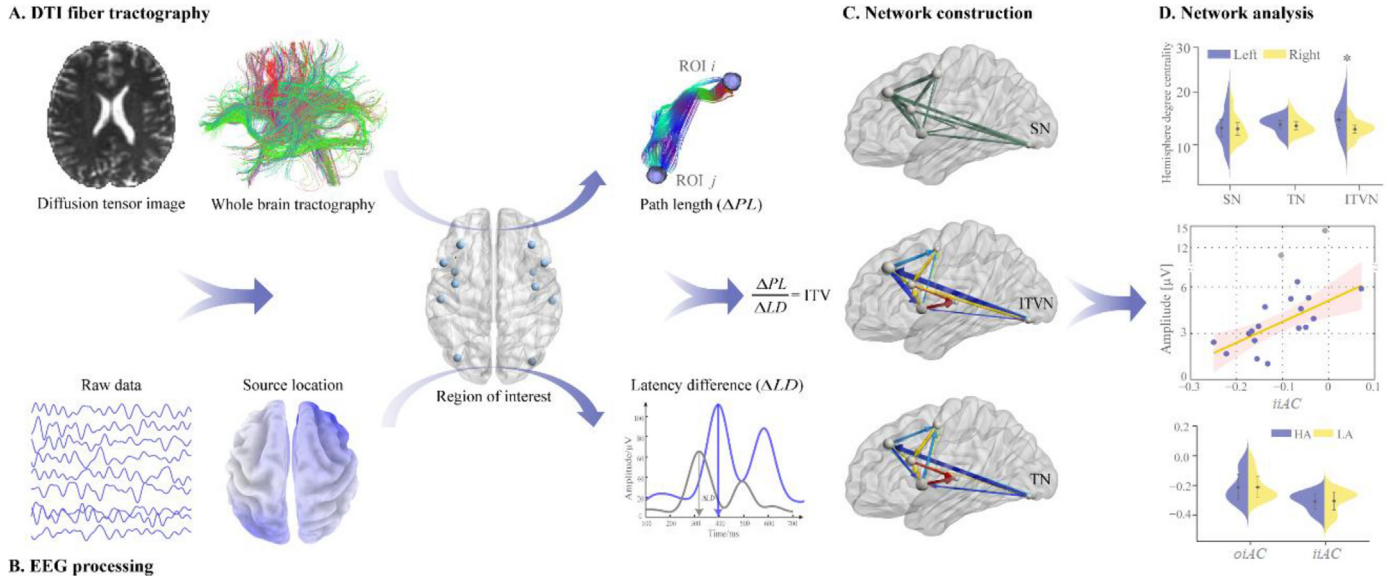

Fig. 1. Pipeline for ITVN construction by combining multimodal information from EEG and DTI. (a) Fiber tractography. Individual fiber path between each pair of ROIs was tracked to obtain the path length (Δ*PL*). (b) EEG processing. EEG source reconstruction was performed to project scalp EEG into the source activities, and the source-space P300 latency was extracted for each ROI. Then, latency difference (Δ*LD*) was calculated for each pair of ROIs. (c) Network construction. Based on the Δ*PL* and Δ*LD*, information transmission velocity (ITV) was calculated, then the structural network (SN), temporal network (TN), and information transmission network (ITVN) were accordingly constructed by the Δ*PL*, Δ*LD*, and ITV, respectively. (d) Network analysis. Hemisphere degree centrality (*HDC*) was calculated for the SN, TN, and ITVN, respectively. Finally, network properties (such as ii*AC* and oi*AC*) were calculated to probe the dynamical diversity of the network and its relationship with P300.

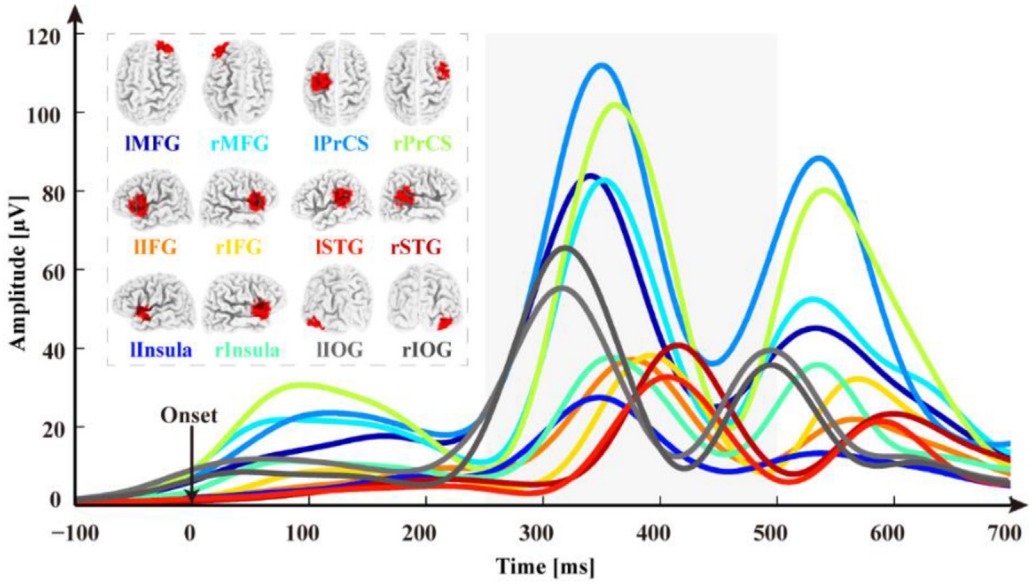

Fig. 2. Grand-averaged P300 waveform across all participants in the source space. Colored lines denote estimated grand-average ERP in different ROIs.

network (TN) were also constructed by the Δ*PL* and Δ*LD* to measure the information transmission mechanism of the human brain (Fig. 1c). Finally, statistical analysis was applied to probe the relationship between transmission network and P300 amplitudes (Fig. 1d), an index that can reflect attention resource allocation (Li et al., 2018).

2.2. Dynamic hierarchical patterns based on the temporal sequence

We first obtained the source-space-projected P300 waveform for each ROI. Fig. 2 shows the grand-averaged P300 waveform for each ROI in the source space. As expected, there was P300 activity in all ROIs within a time interval of [250 500] ms after target onset. Generally, the temporal organization of the network is a general characteristic of human cognition that exists on a wide range of spatiotemporal scales (Vidaurre et al., 2017; Yi et al., 2021). We thus assumed that there are specific temporal patterns of subnetwork configurations underlying the P300 task, and these transitions of subnetworks are dynamically operated and organized in a hierarchical manner. To reveal the hierarchical architectures during the P300 process, we combined both temporal information and spatial distribution to subdivide the hierarchical modules. Thus, for each participant, the P300 latency was extracted from each ROI. P300 peaked on average (± STD) at 370.29 ± 84.18 ms. As seen in Fig. 3a, when the infrequent target stimulus occurred, the information transmission underlying P300 was initiated in the bilateral IOG. Subsequently, the MFG, insula, and PrCS were actively involved in the propagation circuit, while the corresponding responses in the IFG and STG were elicited relatively late.

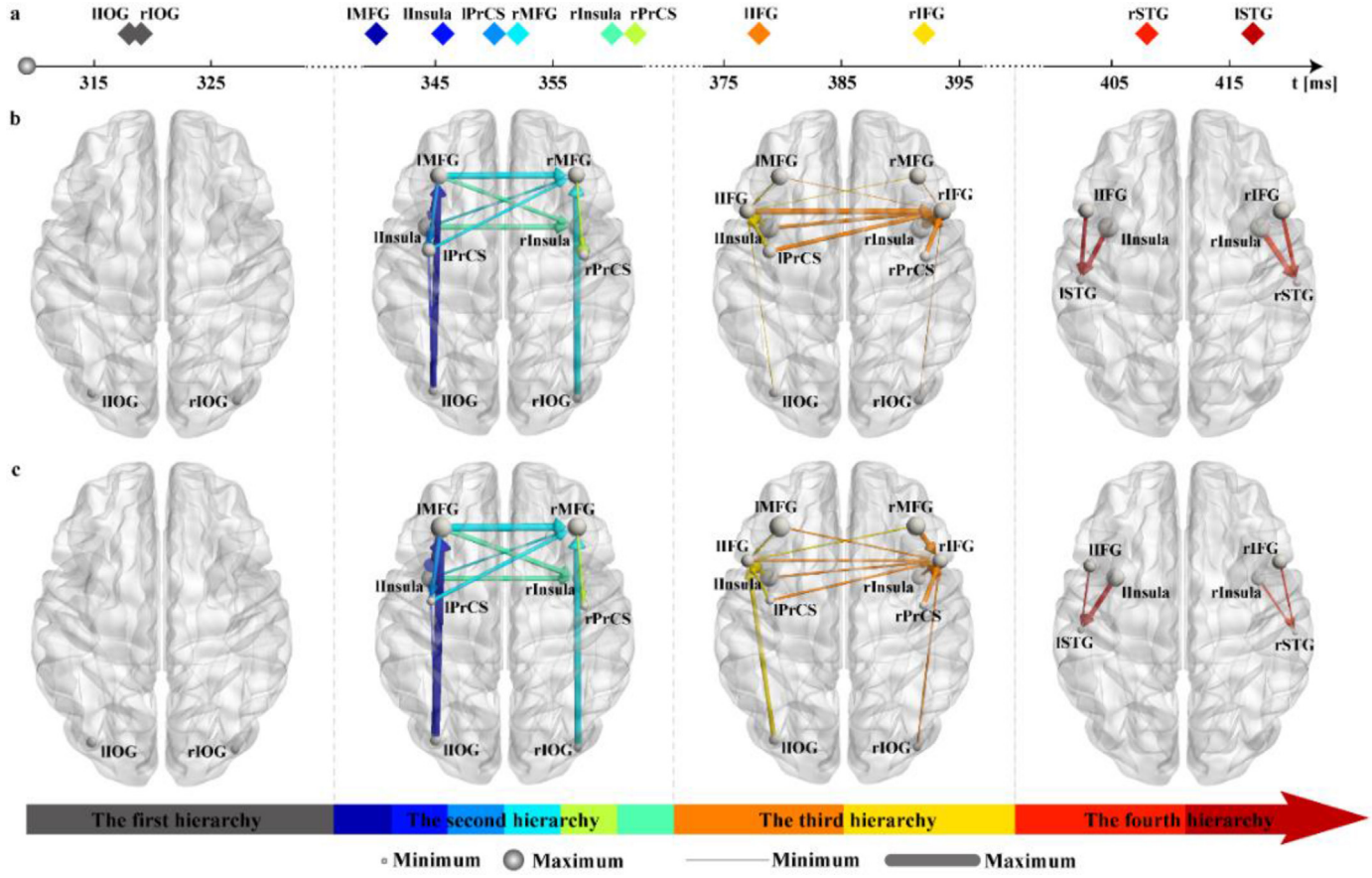

Fig. 3. Dynamic hierarchical network patterns of P300 information transmission. (a) P300 peak latency in source space of 12 ROIs. (b) Temporal network (TN). (c) Information transmission network (ITVN). In (b) and (c), gray spheres indicate the degree centrality (*DC*) of each ROI, with sphere size indicating the importance of this node. Colored lines denote between-ROI flows, arrows indicate the direction of flow, and line thickness represents estimated transmission velocity, that is, the thicker the line, the higher the velocity. The colors of lines indicate to which hierarchical structure the corresponding edges belong. Specifically, IOG of the left and right hemispheres was defined as the first hierarchy, which quickly transmits cognitive information to MFG, Insula, STG, and PrCS of the left and right hemispheres, forming the second hierarchical organization. Thereafter, information flows were unified and integrated into IFG and then propagated to STG, which formed the third and fourth hierarchies, respectively.

As derived from the P300 latency, the TN can be divided into four hierarchical subnetworks with dynamic sequences in Fig. 3b. Meanwhile, according to the definition of ITV, the ITVN (Fig. 3c) had an identical structure of four hierarchical modules as the TN, where the main difference was the distinct transmission velocity between the two networks. As seen in Fig. 3b and Fig. 3c, the source regions, that is, the bilateral IOGs were defined as the first hierarchy of the TN and ITVN, which quickly transmitted information to the MFG, Insula, STG, and PrCS of the left and right hemispheres, forming the second hierarchical organization. Thereafter, the corresponding information was further integrated into the IFG and then propagated to the STG, which formed the third and fourth hierarchy, respectively. Although both ITVN and TN exhibited the same hierarchical structures, the two networks showed different propagation velocities in those four sequential modules. For example, information flowed from the left IFG to the right IFG and from the right Insula to the right STG were relatively fast in the TN, whereas the corresponding ITV in the ITVN was slower. The detailed dynamic information propagation of the four sequential modules is visually shown in the Supplemental Movies.

2.3. Comparisons between transmission networks

Based on the inter-ROI PL, the SN of P300 was constructed and exhibited in Fig. 4a. It appeared that fiber tracts connecting contralateral ROIs exhibit longer path lengths than those of the ipsilateral ROIs. Thereafter, the dynamic hierarchical networks of the TN and ITVN are integrated and presented in Fig. 4b and Fig. 4c to explore the overall transmission mechanism. Specifically, three networks presented distinct spatial patterns of information transmission, such as connectivity between the left PrCS and right MFG, between the right IOG and right IFG, and between the right IFG and right insula. Afterward, network lateralization was investigated for the three networks in Fig. 4, which is quantified by the hemisphere degree centrality (*HDC*). Results showed that the left hemisphere *HDC* of the ITVN was significantly larger than that of the right hemisphere ($t = 2.43$, $p < 0.05$), whereas no significant difference was uncovered in the SN and TN (Fig. 5).

2.4. Relationship between transmission networks and P300 amplitude

We further explored the relationships between transmission velocity networks (i.e., network properties) and P300 metrics (i.e., P300 amplitudes), which are shown in Fig. 6. Considering the directivity of information transmission, the SN was excluded in the following analysis, and the assortativity coefficient (*AC*) was calculated for TN and ITVN, respectively. In fact, as for the physiological signals, it is inevitable to introduce outliers characterized by the large obvious bias from other normal signals (Blankertz et al., 2010; Reinhart et al., 2011), and the outliers will distort or undermine the potential relationship. Thus, it is necessary to find a strategy, e.g., Malahanobis distance (De Maesschalck et al., 2000), to reliably and clearly define the outliers. Herein,

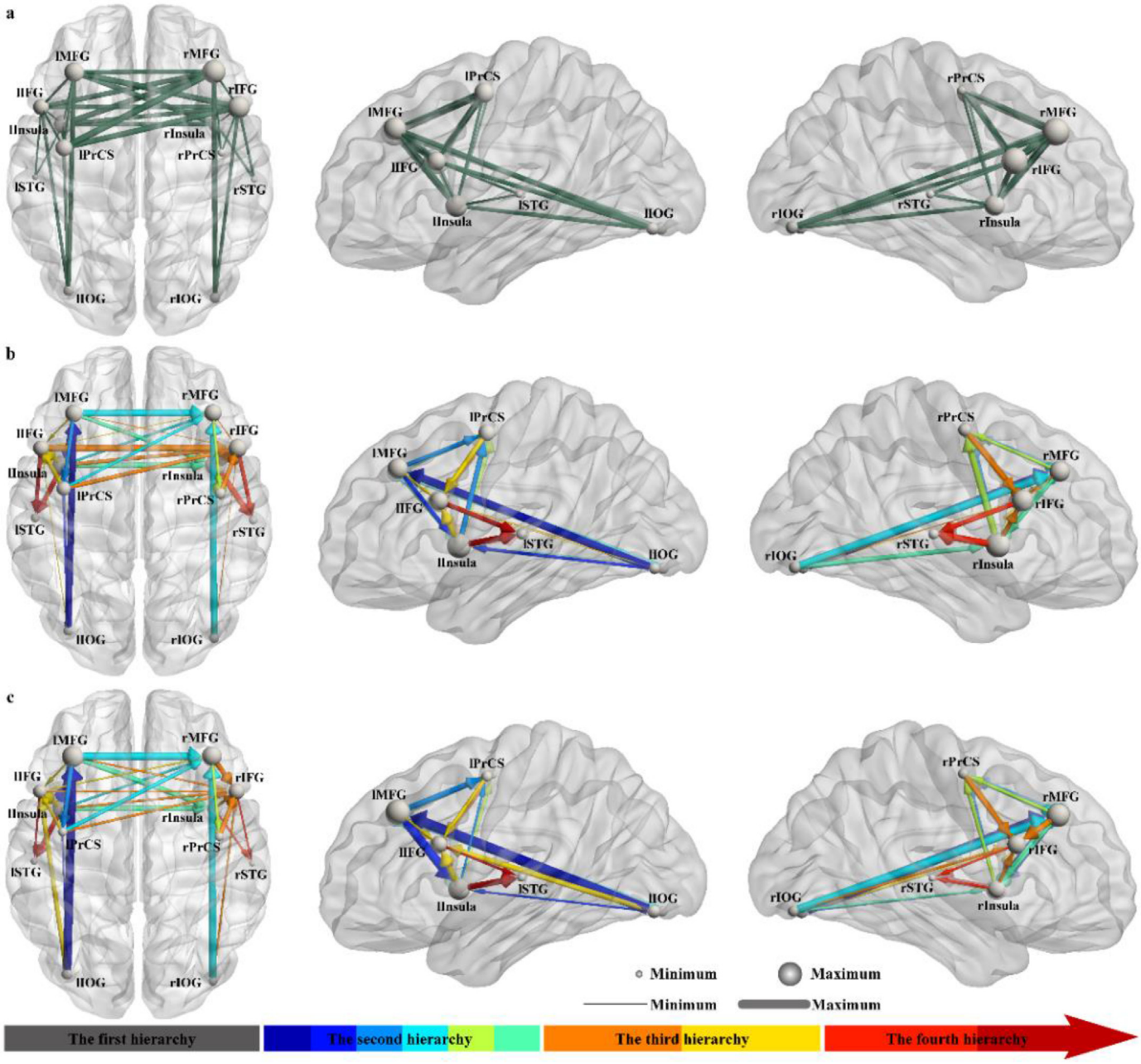

Fig. 4. Information transmission network of P300. (a) Structural network (SN). (b) Temporal network (TN). (c) Information transmission network (ITVN). In each subfigure, gray spheres indicate the degree centrality (*DC*) of each ROI, with sphere size indicating the importance of the node. Colored lines indicate between-ROI flows, arrows indicate the direction of flow, and line thickness represents estimated transmission velocity, that is, the thicker the line, the higher the velocity. In b and c, arrows indicate the direction of information flow. The colors of lines indicate to which hierarchical structure the corresponding edges belong.

following the protocols adopted to define the distorted samples by using Malahanobis distance (Blankertz et al., 2010), two outliers with the 20% largest Malahanobis distance to the data center were then excluded from the following analysis. As displayed in Fig. 6, the P300 amplitude was significantly and positively correlated with the oi*AC* ($r = 0.62$, $p = 0.01$) and ii*AC* ($r = 0.69$, $p = 0.00$) of the ITVN (Fig. 6b), while no significant correlation between network properties and P300 amplitude (oi*AC:* $r = -0.04$, $p = 0.88$; ii*AC:* $r = 0.09$, $p = 0.72$) was verified in the TN (Fig. 6a). Then, the underlying distinctions in network properties between the low and high P300 amplitude groups (LA and HA group, respectively) were investigated. This analysis showed that the HA group had significantly larger oi*AC* and ii*AC* of the ITVN than the LA group (Fig. 7b; oi*AC:* $t = -2.43$, $p < 0.05$; ii*AC:* $t = -1.89$, $p < 0.05$), while no significant difference was seen in the TN (Fig. 7a).

2.5. P300 amplitude prediction by the ITVN properties

Considering that the ITVN properties were highly related to the P300 amplitude (Fig. 6b), the network properties (oi*AC* and ii*AC*) may serve as credible features to predict individual P300 amplitude in the visual oddball task. Hence, in this study, a multivariable linear regression model was established to predict individual P300 amplitudes. And Fig. 8 thereby illustrates the relationship between actual and predicted P300 amplitude, where the *Y*- and *X*-axes indicate the actual and pre-

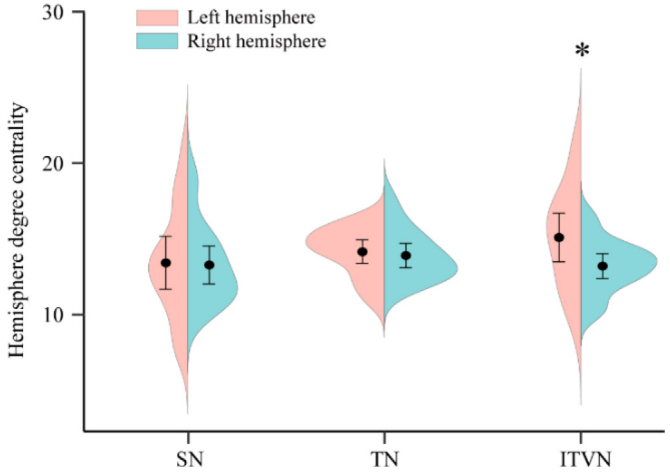

Fig. 5. Hemisphere degree centrality (*HDC*) of left and right hemispheres in SN, TN, and ITVN. Black solid circles show mean values of left or right *HDC* for all participants. Error bars indicate standard errors. * represents $p < 0.05$.

dicted P300 amplitude of these participants, respectively. The corresponding Pearson's correlation coefficient was $r = 0.63$ ($p = 0.00$), along with $RMSE = 1.93$ and $nRMSE = 0.36$, indicating a good prediction power.

3. Discussion

The neural mechanisms underlying high-level human cognition in terms of structural and functional networks have been widely investigated (Hu et al., 2021; Lu et al., 2020). However, due to the lack of an effective method, the information transmission mechanism based on the hierarchical configurations has not been explored yet. In the present study, focusing on the tough challenges of information transmission efficiency estimation in the human brain in vivo, spatial-temporal information derived from the structural dMRI and scalp EEG was, therefore, fused, and a transmission velocity estimation approach, ITV, was accordingly proposed. Based on this, a novel cortical ITVN construction workflow was further developed. The application to a real MRI-EEG dataset (P300) was performed to demonstrate the feasibility and robustness of ITV for cortical ITVN construction and to explore how cognitive information dynamically and hierarchically interacts across brain areas during the P300 generation. Finally, the underlying relationship between the ITVN and P300 component was assessed to probe the inter-individual P300 variability from the information transmission efficiency perspective.

As exhibited in Fig. 2, the cortical time series after reconstruction retains the intrinsic P300 information evoked by task stimulation and can be adopted for the following analysis. Subsequently, based on the workflow of network construction, three types of information transmission networks, SN, TN, and ITVN, were constructed and exhibited in Figs. 3 and 4. As illustrated, the timely and effective delivery of information is crucial to the proper functioning of the nervous system and plays a critical role in accomplishing the required task. The previous study found that when the signal was propagated from one brain site to another, although the signals traveled various fiber paths that have different lengths, their conduction times were quite similar (Pelletier and Pare, 2002). This suggested that longer fiber tracts in Fig. 4a may correspond to a faster ITV. In essence, the brain consists of numerous functional units. When a signal is transmitted to different brain sites, the information may arrive at the end site at different times, which forms precise sequential control similar to that in the circuit system. For instance, taking the fiber tract length in the SN as the reference (Fig. 4a), we can see that fibers projected from one site (e.g., the left MFG) to other sites are of different lengths, and the TN in Fig. 4b also displays irregular transmission time with dynamic directions. This variation in both the fiber tract and propagation delay further infers that the accurate estimation of ITV requires the combination of both variates, and the structural path can provide furnishing constraints or prior approximations (Pillai and Jirsa, 2017).

As shown in Fig. 4c, when both distance and time delay were taken into account, the ITVN exhibited a distinct network pattern from the SN and TN. For instance, SN had very fast velocity estimation between the left PrCS and right MFG, as well as between the right IOG and right IFG due to the long fiber path between them, while TN estimated very slow velocity on account of its long transmission time delay; however, ITV considered both the distance and time factors for transmission velocity calculation and reached a medium velocity estimation. It is the different metrics used to measure transmission velocity that led to the different network patterns shown in Fig. 4.

As reported in related electrophysiological studies, information transmitted across neurons is essentially realized by ion flow toward a specific direction. Myelinated axons can modulate conduction velocity through their interaction with the myelin sheath, while unmyelinated axons rely more on diameter adjustment and axon depolarization (Chéreau et al., 2017; Cohen et al., 2020). Besides, experience-dependent activity modifies the length of myelin internodes along axons, which allows for variations in conduction velocities that provide a degree of plasticity according to environmental needs (Etxeberria et al., 2016). Due to the limitations of current neuroimaging techniques, non-invasive measurement of the ITV along the brain fiber tract is extraordinarily difficult, further resulting in the lack of the gold criteria to evaluate which approach can estimate the ITV most accurately. In the following sections, we further discussed the superiority of ITVN in evaluating the brain's information transmission efficiency from a general physiological basis.

3.1. Faster ITV involving IOG and MFG

The transmission velocity measured with the three different approaches (Fig. 4) consistently exhibited higher velocity between the IOG and MFG in both hemispheres, between bilateral MFG, and between the left MFG and right insula, compared with the information propagation across other brain areas. In essence, in our daily lives, the efficient and accurate delivery of visual information is beneficial and necessary for quick judgment and appropriate response to the surrounding environment. Additionally, attention plays a crucial role in the cognitive processing of P300. The MFG is a processing center related to high attentional load, and the activity in the MFG has a crucial role in maintaining the integrity of attention networks (Gogulski et al., 2017). Hence, these cognitive activities may regulate myelin internode length along axons to alter action potential conduction velocity (Etxeberria et al., 2016). Moreover, human visual cortices and cortical areas next to the MFG have been identified to be heavily myelinated (Abdollahi et al., 2014; Glasser and Van Essen, 2011), which therefore allows for rapid information propagation between these brain regions.

3.2. Left hemisphere dominance of the ITVN

Apart from these similar strong linkages, there exist distinct spatial patterns among the three networks, resulting in different emphasis on the brain hemisphere. As shown in Fig. 3, almost all interhemispheric information transmission was initiated from the left hemisphere to the right one, suggesting that information processing was more prominent in the left hemisphere. Besides, *HDC* was assessed in Fig. 5 to quantify the hemispheric emphasis of information propagation. The result shows that the left hemisphere of the ITVN exhibited a significantly larger *HDC* than that of the right one, whereas no significant difference was discovered in SN and TN. As reported previously, along with brain expansion through evolution, the consumption of intra- and interhemispheric communication gradually becomes too burdensome, leading to increased

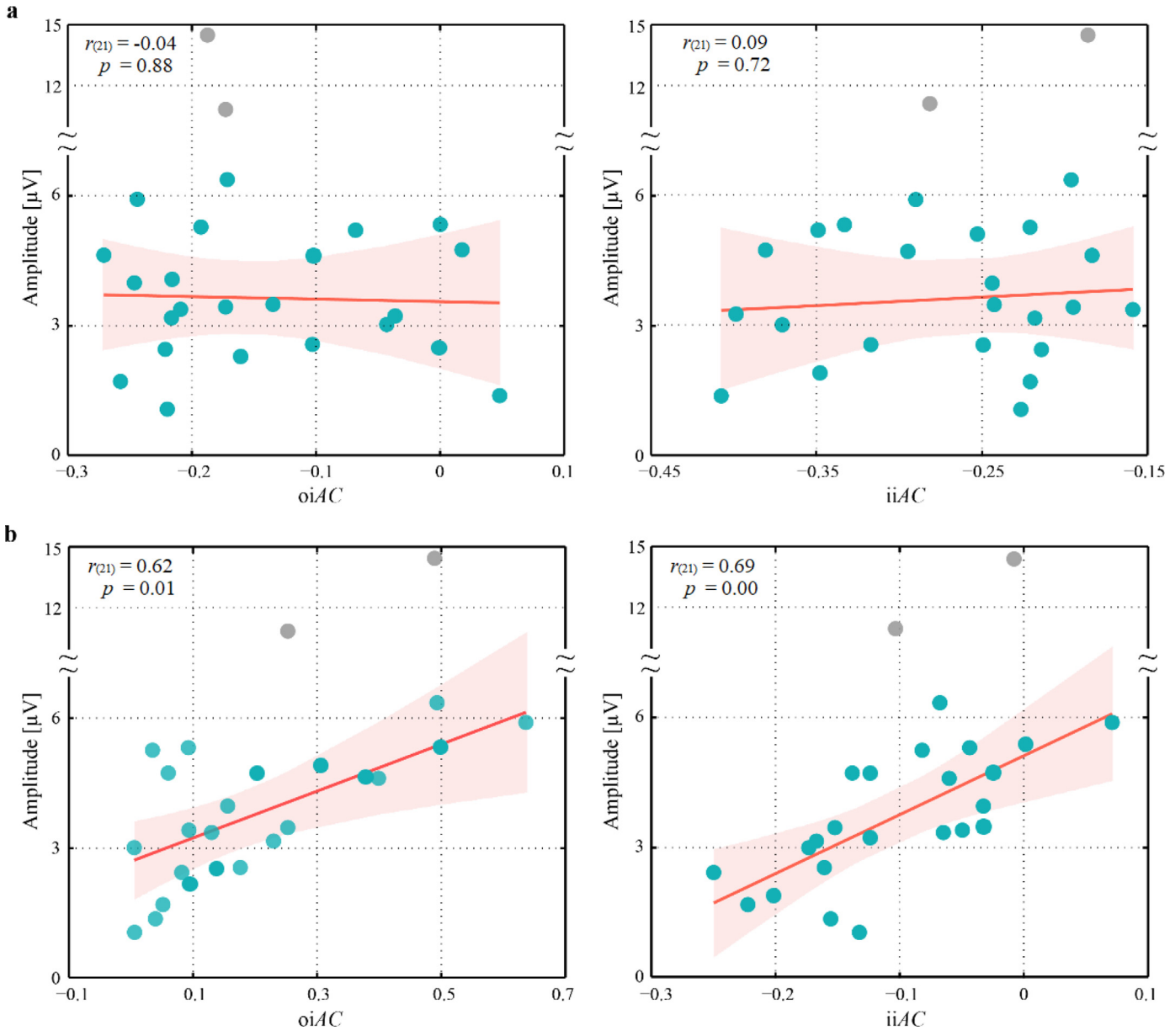

Fig. 6. Relationships between network properties and P300 amplitude. (a) Correlations between TN properties and P300 amplitude. (b) Correlations between ITVN properties and P300 amplitude. In each subfigure, light blue-filled circles denote participants, gray-filled circles denote excluded participants, the pink-solid line is the fitted curve between two variables, and the pink shadow denotes a 95% confidence interval.

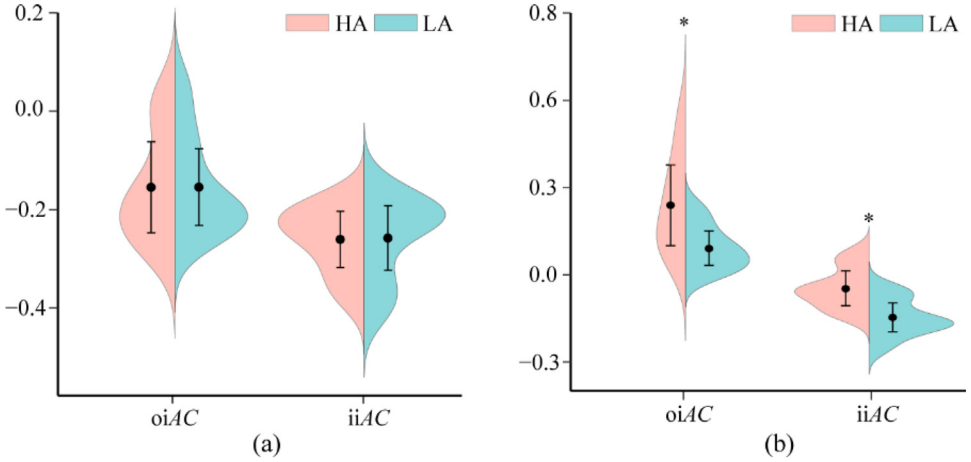

Fig. 7. Differences in network properties between HA and LA groups. (a) Violin plot of network property distribution of TN. (b) Violin plot of network property distribution of the ITVN. Black-solid circles show mean values of network properties for participants with relatively low and high P300 amplitudes. Error bars indicate standard errors. * represents $p < 0.05$. HA-high amplitude group, LA-low amplitude group.

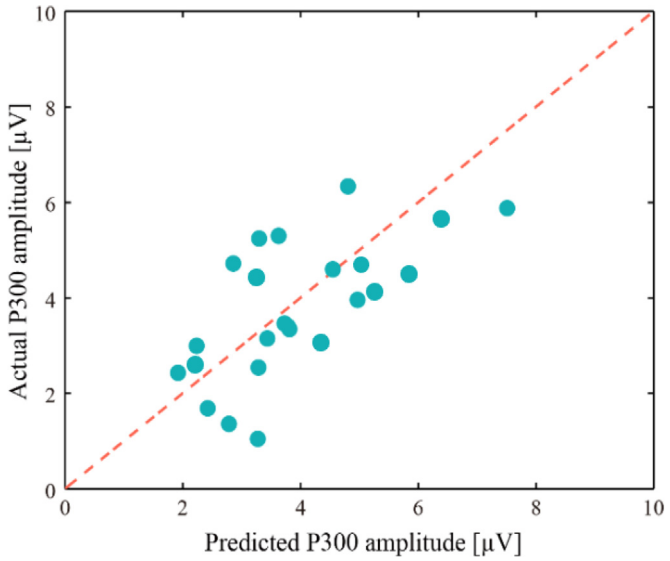

Fig. 8. The relationship between predicted (*X*-axis) and actual (*Y*-axis) P300 amplitude. The light blue-filled circles denote the subjects.

functional modularity within or across hemispheres, and further resulting in functional and anatomical lateralization (Ringo et al., 2015). The left and right hemispheres, therefore, separately specialize in certain cognitive functions. Concerning the present study, all recruited participants were right-handed, their left hemisphere is believed to be reliably and consistently superior to the right one in multiple brain functions, such as global topological perception (Wang et al., 2007), skilled movement, and analytical time sequence processing (Schluter et al., 2001). In this regard, ITVN captured the intrinsic nature of left-hemisphere dominant information propagation underlying P300 in the right-handed participants, whereas the SN and TN failed.

3.3. Hierarchical organization patterns of P300 information transmission

Previous research has shown that visual attention tasks such as oddball detection involve feature-dependent bottom-up and goal-directed top-down attention, which collaborate to accomplish the task (Corbetta and Shulman, 2002). In our work, the time-varying hierarchical modules in Fig. 3 may further account for the importance of bottom-up and top-down attention and the resource shift rule between them. Specifically investigating Fig. 3a and 3b, target-specific processing involving discrimination of task-relevant features (e.g., shape) begins from the visual cortex (Stevens et al., 2000), the bilateral IOG thereby served as source regions and formed the first hierarchical structure.

As for the second module, a strong bottom-up information flow was quickly propagated to the left MFG to allocate attention resources (Chang et al., 2014), which was then merged into the left insula for the maintenance of the target template in working memory (Jiang et al., 2000). Based on the top-down template of the attentional control setting (the target signal) in the current task, our brain would subsequently match the related stimulus. Then, information flows stemming from the left MFG and insula were exerted to the left PrCS for goal-directed response selection (Shulman and L., 2003). When the current stimulus template was consistent with the top-down signal template, the participant's attention could be automatically captured, and the target stimulus could be identified. Interestingly, it was not until the activation of the right MFG that cognitive information began to interact between bilateral hemispheres. In this regard, the response of the right MFG was not only derived from the information flow from the right IOG, but was also affected by that from the left MFG, insula, and PrCS. Thereafter, enhanced information interaction between two hemispheres appeared as the right insula, and PrCS were sequentially activated by contralateral and ipsilateral information flows to match the current stimulus and the top-down signal template.

Generally, the right IFG was presumably important for rapid adaptation in response to currently relevant and salient stimuli (i.e., target stimuli) (Hampshire et al., 2010) based on the top-down signal template. Hence, in the third module, the right IFG may serve as a crucial integral hub to assemble related brain resources, resulting in the most extensive feeding of information flows into it. Moreover, the IFG was found to have extensive fiber connections with other brain regions (Kamali et al., 2014), further manifesting the abundant information flows across the IFG in Fig. 3. For the last module, the IFG exerted top-down control over sensory regions including the STG to coordinate focal elaborate processing of target stimuli (Chadick and Gazzaley, 2011) and to inhibit other memory representations when attempting to retrieve a target representation (Aron et al., 2004). Overall, the revealed hierarchical patterns of ITVN in the P300 task effectively depicted the temporal sequence of cognitive information propagation and further clarified the transmission mechanism of top-down and bottom-up visual attention.

3.4. Relationship between ITVN and P300 variability

Theoretically, when networks are established by diverse variables with various properties, they also display considerable architecture and dynamical diversity, which can be evaluated by the *AC* (Newman, 2003a). Interestingly, the ITVN presented a significant positive correlation between P300 amplitude and oi*AC*, as well as ii*AC* (Fig. 6b), whereas no significant correlation was verified in the TN (Fig. 6a). Generally, P300 denotes the intensity of cognitive processing and is related to the proportion of attention resources devoted to the task at hand (Dallmer-Zerbe et al., 2020). As *AC* is usually related to more efficient information processing (Boccaletti et al., 2006; Newman, 2003b), a larger *AC* consistently illustrates an increase in task-related information transmission, which thereby indexes an increase in brain response to task stimuli, such as a higher P300 amplitude. Moreover, after dividing participants into HA and LA groups, we identified larger oi*AC* and ii*AC* in the HA group than that in the LA group (Fig. 7b, $p < 0.05$), whereas that of the TN did not exhibit this difference (Fig. 7a). As such, the ITVN was better apt at capturing the intrinsic cognitive activities of the brain, and during the P300 tasks, the superior ITVN efficiency of the HA group contributed to the reasonable allocation of task-related resources, especially attention ones. This facilitated task performance, such as higher P300 amplitudes.

The relationship between ITVN properties and P300 amplitude, as well as the properties differences between HA and LA groups, raised a problem of whether individual behavioral variability results from the difference of inter-regional ITV. Hence, multivariable linear regression analysis was applied to predict individual P300 amplitudes. As provided in Fig. 8, the light blue-filled circles distributed along the pink dashed diagonal line (the ideal prediction) validate the ability of the present model in detecting the inter-individual variability in P300 amplitudes. Current results suggest that individual variability in P300 may be attributed to the difference in the brain's information transmission efficiency. And further, the ITVN analysis will also explain the huge variations in brain-computer interface (BCI) performances and help develop credible biomarkers to predict the potential for personalized control of BCIs, as well.

In essence, considering our proposed ITV can effectively measure the information transmission efficiency and the dynamic information transmission hierarchy modules in the human brain, in the future, this will be also applied in related clinical research to learn how the transmission efficiency in brain circuits attenuates, as well as how the ITV networks related to clinical diseases are progressively dysfunctional. Considering the different experimental environments, conditions of stimulation, subject states, and levels of arousal across different works, no consensus to date has been achieved on the source of P300, localizing the matched sources of the current experiment may be an optimal choice for us to

accomplish the ITV analysis. In the meantime, by projecting the scalp EEG components into the source space, choosing reliable methods will greatly affect the findings; if the misattribution of time courses to related cortical sources is introduced, the hierarchical patterns and information transmission network of P300 would be heavily influenced, which will lead to the misunderstanding of the dynamic hierarchical processes of P300. In the future, more attempts at localizing the P300 sources, e.g., developing new source localization methods by adopting a deep learning strategy, will be achieved to validate the reliability of the proposed ITV, and besides the P300 task, the developed approach will be further applied to other cognition tasks including working memory, decision making and emotions to probe the related velocity network patterns.

4. Conclusion

In this study, we proposed a pairwise connectivity measurement termed ITV to map the dynamic hierarchical interaction within the brain, which was further applied to the real P300 MRI-EEG dataset of healthy humans. As reported, clinical neurodegenerative disorders, such as epilepsy and Alzheimer's disease, involve alteration in neuronal function and aberrant circuit activity, further leading to reduced circuit transmission efficiency (Dulla et al., 2016). Understanding how this attenuation of transmission efficiency in brain circuits and networks related to progressive dysfunction may yield insights into the neuropathological mechanism of these diseases. In this regard, our developed approach could evaluate information transmission efficiency, and the capture of the dynamic information transmission hierarchy modules in the human brain. Such abundant and multifaceted information may provide us with new theoretical interpretations for brain disease, and mine the specific biomarker for multiple cognitive degenerations from the transmission velocity perspective.

5. Materials and methods

5.1. Participants

Twenty-five healthy postgraduates (4 females, aged 25.64 ± 1.65 years) were recruited to participate in our present experiment, under the approval of the Institutional Research Ethics Board of the University of Electronic Science and Technology of China. And the reference number of the ethical approval was 106142021030909. As requested, all of them provided written informed consent before the experiment. None of them had any family or personal history of psychiatric or neurological disorders.

5.2. Experimental protocol

A classical visual oddball experiment including 3 runs of P300 tasks was conducted in our study. Each run contained 35 target stimuli (downward-oriented triangle with a thin cross at its center) and 175 standard stimuli (upward-oriented triangle with a thin cross at its center) delivered in a pseudorandom order. As for each trial, a bold cross appeared and lasted 250 ms to alert participants to pay attention to the computer screen, then, a thin cross appeared. Five hundred milliseconds later, a target or standard stimulus was exhibited for 500 ms, during which participants were required to press the "4″ key once noticing the presence of the target stimulus. Afterwards, a black screen lasting 750 ms was exhibited to offer a short rest.

5.3. MRI-EEG acquisition

All images were acquired on a 3.0 T MRI scanner (GE DISCOVERY MR750, USA) using an eight-channel, standard, whole-head coil. DTI was collected by a single-shot spin-echo planar imaging sequence (echo time = 63.6 ms, repetition time = 8500 ms, flip angle =90°, field of view = 256 mm × 256 mm, matrix = 128 × 128, voxel size = 2.0 mm × 2.0 mm × 2.0 mm, 77 slices covering the whole brain). Eight unweighted (b = 0 s/mm^2) and 68 diffusion-weighted (b = 1000s/mm^2) image volumes were recorded. The visual stimuli were presented using E-prime 2.0 software (Psychology Software Tools, Inc., Sharpsburg, PA, USA) and projected onto a screen viewed by the participants via a mirror attached to the head coil. Using Curry 7 (Neuroscan, Charlotte, NC, USA), EEG signals were recorded with 64 Ag/AgCl channels (the 10–20 system). Electrooculogram and electrocardiogram were monitored by two additional channels. Channels AFz and FCz are set for ground and reference, respectively. The impedance per electrode was kept consistently below 5 kΩ, and the online sampling rate was 2000 Hz.

5.4. Estimating information transmission velocity

We applied a new pairwise connectivity measurement termed ITV to define the dynamic interaction within the ITVN of P300. This was defined by the path length of the DTI fiber tracts and the propagation interval derived from cortical EEG at two concerned ROIs. Specifically, the average length of fiber tracts connecting pairwise ROIs was calculated and then defined as the path length ΔPL_{ij}, which was regarded as the physical distance of related information transmission. The latency difference ΔLD_{ij} of cortical EEG signals between pairwise ROIs was then calculated to determine the transmission sequence and how long information propagation takes. ΔLD_{ij} was calculated by subtracting the latency of ith ROI from that of jth ROI, where jth ROI was supposed to have the longer latency. Finally, for the ith and jth ROIs, the ITV from the ith to jth ROI is defined as

$$ITV_{ij} = \frac{\Delta PL_{ij}}{\Delta LD_{ij}} \tag{1}$$

where i and j denote the ith and jth ROI, and $i \neq j$. ΔPL_{ij} and ΔLD_{ij} denote the path length and the latency difference between activation in roi_i and roi_j, respectively. Physiologically, the ITV represents the directed distance of information flow through the fiber tract in unit time from ith to jth ROI, and a larger ITV corresponds to faster information transmission across pairwise ROIs. The detailed definition and calculation regarding ΔPL and ΔLD are depicted below.

DTI fiber tractography. The FMRIB Software Library toolbox [23] was adopted for DTI preprocessing. First, nonbrain tissue was removed by the Brain Extraction Tool. The eddy current-induced distortions and head motion were corrected by the FMRIB Diffusion Toolbox, while the corrected parameters were applied to rotate the gradients. The fractional anisotropy (FA) images were generated by fitting a tensor model at each voxel of the diffusion data, and the diffusion tensors were estimated according to the corrected gradients. Then, the whole-brain fibers were tracked using a continuous tracking algorithm embedded in the DiffusionKit (Xie et al., 2016). Thereinto, path tracing proceeded until either the angle > 45° or FA < 0.1. Thereafter, fiber tracts linking each pair of ROIs were extracted by logical AND concatenation of the two ROIs. Fibers with obvious false paths were discarded. As such, the path length (PL) between roi_i and roi_j was computed by averaging the lengths of all fibers connecting roi_i and roi_j, which is a basic measure that characterizes the physical distance of information transmission and can be expressed as ΔPL_{ij}, where $i \neq j$.

EEG data analysis. EEG signals were first preprocessed by Curry 7 to remove the ballistocardiogram and gradient artifacts following previous procedures (Li et al., 2020a), which was then referenced by the Reference Electrode Standardization Technique (REST) (Yao, 2001) and bandpass filtered ([1, 6] Hz) (Li et al., 2015). Then, 1024 Hz downsampling, [−200, 800] ms data segmentation (0 ms denotes the appearance of target stimulus), [−200, 0] ms baseline correction, and artifact trial removal (±75 μV as the threshold) were adopted. For each participant, the remaining target trials were averaged to achieve an ERP signal.

In contrast to dipole source localization, distributed source imaging does not emphasize the number of sources, instead, a large number of

equivalent dipoles are defined and spatially distributed over the cortical layer (Michel and He, 2019), along with the strengths of these dipoles being estimated accordingly. In essence, multiple distributed source imaging methods, e.g., standardized low-resolution electromagnetic tomography (sLORETA) (Pascual-Marqui, 2002) and minimum norm estimation (MNE)(He et al., 2011), are developed and widely used (Bocquillon et al., 2011). Among these methods, previous studies consistently validate that sLORETA achieves the lowest localization errors and the lowest amount of blurring (Grech et al., 2008; Pascual-Marqui, 2002). Further, sLORETA has also been identified as an efficient tool for functional mapping, as it is consistent with physiology and capable of correct localization, which greatly contributes to its wide applications in recent studies (Imperatori et al., 2014; Keeser et al., 2011).

Concerning our present study, as reported previously, the P300 sources are spatially distributed on the cortical layer (Li et al., 2020a, 2009), and these sources closely interact with each other, forming the generator network of P300. Some approaches, such as MNE, have been proven to be challenged if underlying sources are correlated with each other (Michel and He, 2019). Therefore, in our present study, when accomplishing the cortical source localization, sLORETA was accordingly used to acquire the distributed cortical activities of P300. Moreover, to guarantee the reliability of the source localization, no arbitrary factors had been introduced and related parameters were calculated relying on the scalp EEG adaptively, that is, the weights of these sources were calculated and attributed by the sLORETA without arbitrary manipulation, as well. Herein, based on the EEG epochs averaged across target trials, for each participant, the cortical P300 sources were obtained, and the corresponding reconstructed cortical signals of the P300 were accordingly acquired. Then, the reconstructed time series of each ROI in the source space was extracted as $\boldsymbol{X}_i = [\boldsymbol{x}_1, \boldsymbol{x}_2, ..., \boldsymbol{x}_n]$, where X_i represents the time series set of ith ROI, and x_k $(1 \le k \le n)$ is the time series of kth voxel in the ROI. The n series were averaged to obtain an averaged ERP for roi_i, based on which, P300 latency L_i was calculated as the time point corresponding to the largest positive peak within the time interval of [250 ms, 500 ms] after task onsets (Polich, 2007). We assumed that the information flow is from roi_i to roi_j if the latency from stimuli onset to roi_i is shorter than to roi_j. Then, the latency difference (LD) (i.e., transmission time) between the ith and jth ROIs with direct fiber tract connection can be calculated as $\Delta LD_{ij}=L_j\text{-}L_i$, where $L_j > L_i$, and $i \neq j$.

5.5. Information transmission networks

A network established by graph theory usually comprises a set of edges and nodes. In this work, we set task-related ROIs as nodes, and the weighted edges were ITV between two paired nodes. Therefore, for N ROIs in each participant, corresponding ITVN $\in \mathrm{R}^{N\times N}$ can be calculated as

$$ITVN = \begin{bmatrix} ITV_{11} & ITV_{12} & \cdots & ITV_{1N} \\ ITV_{21} & ITV_{22} & \cdots & ITV_{2N} \\ \vdots & \vdots & \cdots & \vdots \\ ITV_{N1} & ITV_{N2} & \cdots & ITV_{NN} \end{bmatrix} \tag{2}$$

where ITV_{ij} is the ITV between roi_i and roi_j.

Additionally, for comparison, the fiber path length and latency were also considered to construct the transmission network. Hereon, the reciprocal of the LD between pairwise ROIs was defined as $rLD = 1/LD$, forming the weighted edges of the temporal network TN $\in \mathrm{R}^{N\times N}$ as

$$TN = \begin{bmatrix} rLD_{11} & rLD_{12} & \cdots & rLD_{1N} \\ rLD_{21} & rLD_{22} & \cdots & rLD_{2N} \\ \vdots & \vdots & \cdots & \vdots \\ rLD_{N1} & rLD_{N2} & \cdots & rLD_{NN} \end{bmatrix} \tag{3}$$

where rLD_{ij} is the reciprocal of the latency difference between roi_i and roi_j.

Likewise, a structural network SN $\in \mathrm{R}^{N\times N}$ was constructed based on the PL as

$$SN = \begin{bmatrix} PL_{11} & PL_{12} & \cdots & PL_{1N} \\ PL_{21} & PL_{22} & \cdots & PL_{2N} \\ \vdots & \vdots & \cdots & \vdots \\ PL_{N1} & PL_{N2} & \cdots & PL_{NN} \end{bmatrix} \tag{4}$$

where PL_{ij} is the path length between roi_i and roi_j.

5.6. Network properties

Thereafter, the degree centrality (DC), hemispheric degree centrality (HDC), and assortativity coefficient (AC) of the weighted matrices were calculated by the brain connectivity toolbox (http://www.nitrc.org/projects/bct/) (Rubinov and Sporns, 2010). Theoretically, for a given node, the corresponding DC is defined as the sum of all afferent and afferent edges. The larger the DC, the more important the node, which is computed as

$$DC_i = \sum_{j=1}^{N} w_{ij} \tag{5}$$

where N indicates the number of all linked nodes, and w_{ij} denotes the connectivity strength between node i and node j.

Based on DC, HDC denoting the connectivity of the unilateral hemisphere can be computed as

$$HDC = \sum_{i=1}^{M} DC_i = \sum_{i=1}^{M}\sum_{j=1}^{N} w_{ij} \tag{6}$$

where M is the number of nodes in the left or right hemisphere.

AC measures the dynamical diversity when networks are established by diverse variables (Newman, 2003a). Specifically, positive AC indicates that this network has a relatively resilient center of mutually interconnected high-degree hubs, while a network with a negative AC has distributed and consequently vulnerable high-degree hubs (Newman, 2002). AC is formulated as

$$AC = \frac{l^{-1}\sum_{(i,j)\in L} K_i^a K_j^b - \left[l^{-1}\sum_{(i,j)\in L}\frac{1}{2}\left(K_i^a + K_j^b\right)\right]^2}{l^{-1}\sum_{(i,j)\in L}\frac{1}{2}[(K_i^a)^2 + (K_j^b)^2] - \left[l^{-1}\sum_{(i,j)\in L}\frac{1}{2}\left(K_i^a + K_j^b\right)\right]^2} \tag{7}$$

where L and l denote the set of all links in the network and the number of links. When a is in, b is in, AC estimates the tendency of original nodes with in-degree to link to target nodes with in-degree (iiAC); while when a is out, b is in, AC quantifies that of the out-degree to link to target nodes with in-degree (oiAC). $K_i^{in} = \sum_{j\in N} w_{ij}$ and $K_i^{out} = \sum_{j\in N} w_{ji}$ denote the in-degree and out-degree of the nodes at both ends of the edge.

5.7. Relationship between transmission networks and P300 amplitude

Given the critical role of P300 in human cognition and its huge variability across individuals, correlations between P300 amplitudes and network properties were first probed by Pearson's correlation analysis. As depicted in Fig. 6, two outliers with the 20% largest Malahanobis distance to the data center were excluded from the following analysis. Then, the remaining participants were ranked from smallest to largest based on their P300 amplitudes. Thereinto, the top twelve participants were allocated to the low amplitude (LA) group, while the bottom eleven participants were allocated to the high amplitude (HA) group. And the underlying differences in network properties between the two groups were evaluated accordingly by the independent-sample t-test.

5.8. Prediction of P300 amplitude based on multiple linear regression model

To further validate the relationships between information transmission efficiency and inter-individual P300 variability, a multivariable linear regression model based on two ITVN attributes (i.e., the oiAC and

ii*AC*) was established as follows, to predict individual P300 amplitudes.

$$AM = \beta_0 + \beta_1 * oiAC + \beta_2 * iiAC + \varepsilon \quad (8)$$

where ε and *AM* are the error term and the P300 amplitude, respectively. $\beta_{0\ldots2}$ are the regression coefficients. Herein, the corresponding prediction performance was evaluated by the leave-one-out cross-validation (LOOCV) strategy (Si et al., 2020). Concretely, within each LOOCV iteration, all participants would be divided into two independent groups, i.e., the training and testing groups; and the prediction model will be trained depending upon the training set, which is then applied to the testing set, to quantify the prediction performance. Assuming we have enrolled *P* participants in this study, within each LOOCV iteration, following the LOOCV procedure, *P*-1 participants will be divided into the training set, and their P300 amplitudes are used to independently train the multivariable linear regression model. The remaining 1 participant is then regarded as the testing set, and his/her P300 amplitude is further input into the trained model, to accomplish this prediction iteration of P300 amplitude. Thereafter, the next LOOCV iteration will initiate until all participants have been served as the testing set for one time. Eventually, the LOOCV validation is finished, and the corresponding P300 amplitude per participant is predicted accordingly.

In the meantime, to further quantify the capacity of the prediction process, following our previous study (Jiang et al., 2022), the root mean square error (*RMSE*) and normalized RMSE (*nRMSE*) were also calculated, to describe the corresponding prediction error.

$$RMSE = \sqrt{\frac{1}{P}\sum_{t=1}^{P}(X_t - Y_t)^2} \quad (9)$$

$$nRMSE = RMSE/\bar{X} \quad (10)$$

where *Y* denotes the predicted P300 amplitude per participant, *X* denotes the actual P300 amplitude per participant, *P* denotes the total number of enrolled participants, and $\bar{X}$ denotes the mean of the actual P300 amplitudes across participants.

Declaration of Competing Interest

The authors declare that they have no financial or competing interests.

Credit authorship contribution statement

Lin Jiang: Conceptualization, Methodology, Formal analysis, Writing – original draft. **Fali Li:** Supervision, Writing – original draft, Writing – review & editing, Funding acquisition. **Zhaojin Chen:** Software, Visualization. **Bin Zhu:** Investigation, Software. **Chanlin Yi:** Data curation, Visualization. **Yuqin Li:** Data curation, Visualization. **Tao Zhang:** Investigation. **Yueheng Peng:** Software, Investigation. **Yajing Si:** Investigation. **Zehong Cao:** Writing – review & editing. **Antao Chen:** Writing – review & editing. **Dezhong Yao:** Writing – review & editing, Funding acquisition. **Xun Chen:** Supervision, Writing – review & editing. **Peng Xu:** Conceptualization, Supervision, Funding acquisition.

Data and code availability statement

The dataset analyzed in the current study as well as scripting and plotting code are available from the corresponding authors via email on request.

Acknowledgments

The authors wish to thank Kimmo Alho for reading and offering comments on an earlier draft of this paper. This work was supported by the National Natural Science Foundation of China (#62103085, #61961160705, #U19A2082), the Science and Technology Development Fund, Macau SAR (File no. 0045/2019/AFJ), the Project of Science and Technology Department of Sichuan Province (#2021YFSY0040, #2020ZYD013), and the Scientific Research Foundation of Sichuan Provincial People's Hospital (2021LY21).

Supplementary materials

Supplementary material associated with this article can be found, in the online version, at doi:10.1016/j.neuroimage.2023.119997.

References

Abdollahi, R.O., Kolster, H., Glasser, M.F., Robinson, E.C., Coalson, T.S., Dierker, D., Jenkinson, M., Van Essen, D.C., Orban, G.A., 2014. Correspondences between retinotopic areas and myelin maps in human visual cortex. Neuroimage 99, 509–524.
Aron, A.R., Robbins, T.W., Poldrack, R.A., 2004. Inhibition and the right inferior frontal cortex. Trends Cogn. Sci. 8 (4), 170–177.
Berkes, P., Orbán, G., Lengyel, M., Fiser, J.J.S., 2011. Spontaneous cortical activity reveals hallmarks of an optimal internal model of the environment. Science 331 (6013), 83–87.
Blankertz, B., Sannelli, C., Halder, S., Hammer, E.M., Kübler, A., Müller, K.-R., Curio, G., Dickhaus, T., 2010. Neurophysiological predictor of SMR-based BCI performance. Neuroimage 51 (4), 1303–1309.
Boccaletti, S., Latora, V., Moreno, Y., Chavez, M., Hwang, D.-U., 2006. Complex networks: structure and dynamics. Phys. Rep. 424 (4–5), 175–308.
Bocquillon, P., Bourriez, J.L., Palmero-Soler, E., Betrouni, N., Houdayer, E., Derambure, P., Dujardin, K., 2011. Use of sLORETA to localize the cortical sources of target- and distracter-elicited P300 components. Clin. Neurophysiol.: Off. J. Int. Fed. Clin. Neurophysiol. 122 (10), 1991–2002.
Bore, J.C., Li, P., Jiang, L., Ayedh, W.M., Chen, C., Harmah, D.J., Yao, D., Cao, Z., Xu, P., 2021. A long short-term memory network for sparse spatiotemporal EEG source imaging. IEEE Trans. Med. Imaging..
Canter, R.G., Penney, J., Tsai, L.-H., 2016. The road to restoring neural circuits for the treatment of Alzheimer's disease. Nature 539 (7628), 187–196.
Chadick, J.Z., Gazzaley, A., 2011. Differential coupling of visual cortex with default or frontal-parietal network based on goals. Nat. Neurosci. 14 (7), 830–832.
Chang, J., Zhang, M., Hitchman, G., Qiu, J., Liu, Y., 2014. When you smile, you become happy: evidence from resting state task-based fMRI. Biol. Psychol. 103, 100–106.
Chéreau, R., Saraceno, G.E., Angibaud, J., Cattaert, D., Nägerl, U.V., 2017. Superresolution imaging reveals activity-dependent plasticity of axon morphology linked to changes in action potential conduction velocity. Proc. Natl. Acad. Sci. U. S. A. 114 (6), 1401.
Cohen, C.C., Popovic, M.A., Klooster, J., Weil, M.-T., Möbius, W., Nave, K.-A., Kole, M.H., 2020. Saltatory conduction along myelinated axons involves a periaxonal nanocircuit. Cell 180 (2), 311–322 e315.
Corbetta, M., Shulman, G.L., 2002. Control of goal-directed and stimulus-driven attention in the brain. Nat. Rev. Neurosci. 3 (3), 201–215.
Dallmer-Zerbe, I., Popp, F., Lam, A.P., Philipsen, A., Herrmann, C.S., 2020. Transcranial alternating current stimulation (tACS) as a tool to modulate P300 amplitude in attention deficit hyperactivity disorder (ADHD): preliminary findings. Brain Topogr. 33 (2), 191–207.
De Maesschalck, R., Jouan-Rimbaud, D., Massart, D.L., 2000. The Mahalanobis distance. Chemometr. Intell. Lab. 50 (1), 1–18.
Demirtaş, M., Burt, J.B., Helmer, M., Ji, J.L., Adkinson, B.D., Glasser, M.F., Van Essen, D.C., Sotiropoulos, S.N., Anticevic, A., Murray, J.D., 2019. Hierarchical heterogeneity across human cortex shapes large-scale neural dynamics. Neuron 101 (6), 1181–1194 e1113.
Dinstein, I., Heeger, D.J., Behrmann, M., 2015. Neural variability: friend or foe? Trends Cogn. Sci. 19 (6), 322–328.
Dulla, C.G., Coulter, D.A., Ziburkus, J., 2016. From molecular circuit dysfunction to disease: case studies in epilepsy, traumatic brain injury, and Alzheimer's disease. Neuroscientist 22 (3), 295–312.
Etxeberria, A., Hokanson, K.C., Dang, Q.D., Mayoral, S.R., Chan, J.R., 2016. Dynamic modulation of myelination in response to visual stimuli alters optic nerve conduction velocity. J. Neurosci. 36 (26), 6937.
Glasser, M.F., Van Essen, D.C., 2011. Mapping human cortical areas in vivo based on myelin content as revealed by T1-and T2-weighted MRI. J. Neurosci. 31 (32), 11597–11616.
Gogulski, J., Zetter, R., Nyrhinen, M., Pertovaara, A., Carlson, S., 2017. Neural substrate for metacognitive accuracy of tactile working memory. Cereb. Cortex 27 (11), 5343–5352.
Grech, R., Cassar, T., Muscat, J., Camilleri, K.P., Fabri, S.G., Zervakis, M., Xanthopoulos, P., Sakkalis, V., Vanrumste, B., 2008. Review on solving the inverse problem in EEG source analysis. J. Neuroeng. Rehabil. 5 (1), 1–33.
Hampshire, A., Chamberlain, S.R., Monti, M.M., Duncan, J., Owen, A.M., 2010. The role of the right inferior frontal gyrus: inhibition and attentional control. Neuroimage 50 (3), 1313–1319.
Hassan, M., Wendling, F., 2018. Electroencephalography source connectivity: aiming for high resolution of brain networks in time and space. IEEE Signal Process. Mag. 35 (3), 81–96.
He, B., Dai, Y., Astolfi, L., Babiloni, F., Yuan, H., Yang, L., 2011. eConnectome: a MATLAB toolbox for mapping and imaging of brain functional connectivity. J. Neurosci. Meth. 195 (2), 261–269.

Horowitz, A., Barazany, D., Tavor, I., Bernstein, M., Yovel, G., Assaf, Y., 2015. In vivo correlation between axon diameter and conduction velocity in the human brain. Brain Struct. Funct. 220 (3), 1777–1788.
Hu, W., Meng, X., Bai, Y., Zhang, A., Qu, G., Cai, B., Zhang, G., Wilson, T.W., Stephen, J.M., Calhoun, V.D., 2021. Interpretable multimodal fusion networks reveal mechanisms of brain cognition. IEEE Trans. Med. Imaging 40 (5), 1474–1483.
Imperatori, C., Farina, B., Quintiliani, M.I., Onofri, A., Gattinara, P.C., Lepore, M., Gnoni, V., Mazzucchi, E., Contardi, A., Della Marca, G., 2014. Aberrant EEG functional connectivity and EEG power spectra in resting state post-traumatic stress disorder: a sLORETA study. Biol. Psychol. 102, 10–17.
Jiang, L., He, R., Li, Y., Yi, C., Peng, Y., Yao, D., Wang, Y., Li, F., Xu, P., Yang, Y., 2022. Predicting the long-term after-effects of rTMS in autism spectrum disorder using temporal variability analysis of scalp EEG. J. Neural Eng. 19 (5), 056044.
Jiang, Y., Haxby, J.V., Martin, A., Ungerleider, L.G., Parasuraman, R., 2000. Complementary neural mechanisms for tracking items in human working memory. Science 287 (5453), 643–646.
Kamali, A., Flanders, A.E., Brody, J., 2014. Tracing superior longitudinal fasciculus connectivity in the human brain using high resolution diffusion tensor tractography. Brain Struct. Funct. 219 (1), 269–281.
Kapanci, T., Merks, S., Rammsayer, T.H., Troche, S.J., 2019. On the relationship between P3 latency and mental ability as a function of increasing demands in a selective attention task. Brain Sci. 9 (2), 28.
Keeser, D., Padberg, F., Reisinger, E., Pogarell, O., Kirsch, V., Palm, U., Karch, S., Moller, H.J., Nitsche, M.A., Mulert, C., 2011. Prefrontal direct current stimulation modulates resting EEG and event-related potentials in healthy subjects: a standardized low resolution tomography (sLORETA) study. Neuroimage 55 (2), 644–657.
Li, F., Chen, B., Li, H., Zhang, T., Wang, F., Jiang, Y., Li, P., Ma, T., Zhang, R., Tian, Y., 2016. The time-varying networks in P300: a task-evoked EEG study. IEEE Trans. Neural Syst. Rehabil. Eng. 24 (7), 725–733.
Li, F., Liu, T., Wang, F., Li, H., Gong, D., Zhang, R., Jiang, Y., Tian, Y., Guo, D., Yao, D., 2015. Relationships between the resting-state network and the P3: evidence from a scalp EEG study. Sci Rep 5, 15129.
Li, F., Tao, Q., Peng, W., Zhang, T., Si, Y., Zhang, Y., Yi, C., Biswal, B., Yao, D., Xu, P., 2020a. Inter-subject P300 variability relates to the efficiency of brain networks reconfigured from resting-to task-state: evidence from a simultaneous event-related EEG-fMRI study. Neuroimage 205, 116285.
Li, F., Yi, C., Jiang, Y., Liao, Y., Si, Y., Yao, D., Zhang, Y., Xu, P., 2018. The construction of large-scale cortical networks for P300 from scalp EEG. IEEE Access 6, 68498–68506.
Li, F., Yi, C., Liao, Y., Jiang, Y., Si, Y., Song, L., Zhang, T., Yao, D., Zhang, Y., Cao, Z., Xu, P., 2020b. Reconfiguration of brain network between resting-state and P300 task. IEEE Trans. Cogn. Dev. Syst. 2 (13), 1.
Li, Y., Wang, L.Q., Hu, Y., 2009. Localizing P300 generators in high-density event-related potential with fMRI. Med. Sci. Monit. 15 (3), MT47.
Linden, D.E.J., 2005. The P300: where in the brain is it produced and what does it tell us? Neuroscientist 11 (6), 563–576.
Lu, Z., Li, Q., Gao, N., Yang, J., 2020. Time-varying networks of ERPs in P300-speller paradigms based on spatially and semantically congruent audiovisual bimodality. J. Neural Eng. 17 (4), 046015.
Michel, C.M., He, B., 2019. EEG source localization. Handb. Clin. Neurol. 160, 85–101.
Morcos, A.S., Harvey, C.D., 2016. History-dependent variability in population dynamics during evidence accumulation in cortex. Nat. Neurosci. 19 (12), 1672–1681.
Newman, M.E., 2002. Assortative mixing in networks. Phys. Rev. Lett. 89 (20), 208701.
Newman, M.E., 2003a. Mixing patterns in networks. Phys. Rev. E 67 (2), 026126.
Newman, M.E., 2003b. The structure and function of complex networks. SIAM Rev. 45 (2), 167–256.
Panzeri, S., Macke, J.H., Gross, J., Kayser, C., 2015. Neural population coding: combining insights from microscopic and mass signals. Trends Cogn. Sci. 19 (3), 162–172.
Pascual-Marqui, R.D., 2002. Standardized low-resolution brain electromagnetic tomography (sLORETA): technical details. Methods Find. Exp. Clin. Pharmacol. 24 (Suppl D), 5–12.
Pelletier, J.G., Pare, D., 2002. Uniform range of conduction times from the lateral amygdala to distributed perirhinal sites. J. Neurophysiol. 87 (3), 1213–1221.
Pillai, A.S., Jirsa, V.K., 2017. Symmetry breaking in space-time hierarchies shapes brain dynamics and behavior. Neuron 94 (5), 1010–1026.
Polich, J., 2007. Updating P300: an integrative theory of P3a and P3b. Clin. Neurophysiol. 118 (10), 2128–2148.
Reed, T.E., Jensen, A.R., 1992. Conduction velocity in a brain nerve pathway of normal adults correlates with intelligence level. Intelligence 16 (3–4), 0–272.
Reed, T.E., Vernon, P.A., Johnson, A.M., 2004. Sex difference in brain nerve conduction velocity in normal humans. Neuropsychologia 42 (12), 1709–1714.
Reinhart, R.M.G., Mathalon, D.H., Roach, B.J., Ford, J.M., 2011. Relationships between pre-stimulus gamma power and subsequent P300 and reaction time breakdown in schizophrenia. Int. J. Psychophysiol. 79 (1), 16–24.
Ringo, J.L., Doty, R.W., Demeter, S., Simard, P.Y., 2015. Time is of the essence: a conjecture that hemispheric specialization arises from interhemispheric conduction delay. Cereb. Cortex 4 (4), 331.
Rubinov, M., Sporns, O.J.N., 2010. Complex network measures of brain connectivity: uses and interpretations. Neuroimage 52 (3), 1059–1069.
Salami, M., Itami, C., Tsumoto, T., Kimura, F., 2003. Change of conduction velocity by regional myelination yields constant latency irrespective of distance between thalamus and cortex. Proc. Natl. Acad. Sci. U. S. A. 100 (10), 6174–6179.
Schluter, N., Krams, M., Rushworth, M., Passingham, R., 2001. Cerebral dominance for action in the human brain: the selection of actions. Neuropsychologia 39 (2), 105–113.
Shekhar, K., Lapan, S.W., Whitney, I.E., Tran, N.M., Macosko, E.Z., Kowalczyk, M., Adiconis, X., Levin, J.Z., Nemesh, J., Goldman, M., McCarroll, S.A., Cepko, C.L., Regev, A., Sanes, J.R., 2016. Comprehensive classification of retinal bipolar neurons by single–cell transcriptomics. Cell 166 (5), 1308–1323 e1330.
Shulman, L., G., 2003. Quantitative analysis of attention and detection signals during visual search. J. Neurophysiol. 90 (5), 3384–3397.
Si, Y., Li, F., Duan, K., Tao, Q., Li, C., Cao, Z., Zhang, Y., Biswal, B., Li, P., Yao, D., 2020. Predicting individual decision-making responses based on single-trial EEG. Neuroimage 206, 116333.
Sousa, A.M.M., Meyer, K.A., Santpere, G., Gulden, F.O., Sestan, N., 2017. Evolution of the human nervous system function, structure, and development. Cell 170 (2), 226–247.
Stevens, A.A., Skudlarski, P., Gatenby, J.C., Gore, J.C., 2000. Event-related fMRI of auditory and visual oddball tasks. Magn. Reson. Imaging 18 (5), 495–502.
Vidaurre, D., Smith, S.M., Woolrich, M.W., 2017. Brain network dynamics are hierarchically organized in time. Proc. Natl. Acad. Sci. U. S. A. 114 (48), 12827–12832.
Wang, B., Zhou, T., Zhuo, Y., Chen, L., 2007. Global topological dominance in the left hemisphere. Proc. Natl. Acad. Sci. U. S. A. 104 (52), 21014–21019.
Xie, S., Chen, L., Zuo, N., Jiang, T., 2016. Diffusion Kit: a light one-stop solution for diffusion MRI data analysis. J. Neurosci. Methods 273 (273), 107–119.
Yao, D., 2001. A method to standardize a reference of scalp EEG recordings to a point at infinity. Physiol. Meas. 22 (4), 693.
Yi, C., Yao, R., Song, L., Jiang, L., Si, Y., Li, P., Li, F., Yao, D., Zhang, Y., Xu, P., 2021. A novel method for constructing EEG large-scale cortical dynamical functional network connectivity (dFNC): WTCS. IEEE T. Cybern.
Zhang, D., Huang, J., Jie, B., Du, J., Tu, L., Liu, M., 2018. Ordinal pattern: a new descriptor for brain connectivity networks. IEEE Trans. Med. Imaging 37 (7), 1711–1722.
Zhu, X., Li, H., Shen, H.T., Zhang, Z., Ji, Y., Fan, Y., 2021. Fusing functional connectivity with network nodal information for sparse network pattern learning of functional brain networks. Inf. Fusion 75, 131–139.